Research Article Vol. 34, No. 8 / 20 Apr 2026 / Optics Express 15406
Optics EXPRESS

Frequency-scanning nonlinearity suppression for FSI ranging based on a phenomenological modeling approach

ZHONGWEN DENG,[1] WENJUN CHEN,[1] XIAWEI MENG,[2] XIN YAO,[3,*] SHUWEI ZHANG,[1] CHENXU WANG,[1] HAIFENG SUN,[1] LIN LI,[4] HENGKANG ZHANG,[4] HAI GONG,[5] LI WANG,[4] XIAOPING LI,[1] AND GLEB VDOVIN[6,7]

[1]*School of Space Science and Technology, Xidian University, Xi'an 710071, China*
[2]*School of Construction Machinery, Chang'an University, Xi'an 710064, China*
[3]*National Time Service Center, Chinese Academy of Sciences, Xi'an 710600, China*
[4]*Space Optoelectronic Measurement and Perception Lab, Beijing Institute of Control Engineering, Beijing 100190, China*
[5]*HIO Technology (Huzhou) Co. Ltd., Huzhou 313000, China*
[6]*Faculty of Mechanical Engineering, Delft University of Technology, Mekelweg 2, 2628CD Delft, The Netherlands*
[7]*School of Instrumentation Science and Engineering, Harbin Institute of Technology, Harbin 150080, China*
[*]*yaoxin@ntsc.ac.cn*

Abstract: Frequency-scanning nonlinearity fundamentally limits the ranging precision of frequency-scanning interferometry (FSI) systems based on external cavity diode lasers (ECDLs). To address this limitation, a frequency scanning nonlinearity suppression method based on a rate-dependent asymmetric Prandtl–Ishlinskii (RA-PI) model is proposed. By employing, for the first time, a phenomenological modeling approach, the rate-dependent and asymmetric nonlinear optical frequency response of the ECDL is accurately characterized. An inverse RA-PI model is derived and implemented as a feedforward compensator to linearize the frequency scanning. Experimental results show that the frequency-scanning linearity is improved by approximately one order of magnitude. Consequently, the maximum standard deviation of absolute distance measurements is reduced from 58.25 μm to 9.79 μm, and the maximum relative displacement deviation decreases from 42.97 μm to 11.56 μm. Furthermore, the velocity measurement precision for dynamic targets is improved by a factor of 2.61 to 5.75.

1. Introduction

Frequency-scanning interferometry (FSI) is a promising technique for absolute distance measurement owing to its high precision, unambiguous measurement capability, and simple system architecture [1–9]. It has been widely employed in diverse applications, including industrial metrology [2,10], aeronautical manufacturing [11,12], autonomous navigation [13,14], and biomedical imaging [8,15]. The performance of an FSI system is primarily determined by the frequency scanning bandwidth of the laser source. Among available tunable laser options, the external cavity diode laser (ECDL) is particularly attractive due to its narrow linewidth and wide mode-hop-free tuning range [16–18]. In an ECDL, optical frequency tuning is typically achieved by adjusting the external cavity length using a piezoelectric actuator (PEA). However, the intrinsic hysteresis and creep effects of the PEA introduce pronounced nonlinearities into the frequency-scanning process [19–21], which degrade phase extraction accuracy and ultimately limit the ranging precision of FSI systems.

#595572 https://doi.org/10.1364/OE.595572
Journal © 2026 Received 15 Feb 2026; revised 1 Apr 2026; accepted 2 Apr 2026; published 15 Apr 2026

Optics EXPRESS

Existing approaches for suppressing frequency-scanning nonlinearity can be broadly classified into post-processing-based and active linearization-based methods. Post-processing approaches commonly employ an auxiliary interferometer to resample the beat signal at equidistant optical frequency intervals [9,22–24]. Although effective, the measurable range is constrained by the optical path difference (OPD) of the reference interferometer according to the Nyquist criterion, and extending the range requires a large OPD, typically implemented using long fiber interferometers, which increase system complexity and reduce environmental robustness. On the other hand, active linearization techniques aim to directly improve the frequency-scanning linearity of the laser source. Optical phase-locked loop based methods have demonstrated excellent linearization performance [25,26], but their implementation requires high-bandwidth electronics, which limits the achievable scanning rate and increases system cost. Feedforward approaches based on iterative learning control (ILC) have also been reported [13], however, the iterative parameter update process significantly prolongs system initialization time. Analytical pre-distortion methods have been proposed from a mechanistic perspective [20,27,28], yet their effectiveness is often limited by simplified assumptions that fail to capture the rate-dependent and asymmetric nature of frequency-scanning nonlinearities.

The root cause of frequency-scanning nonlinearity in ECDLs lies in the rate-dependent and asymmetric displacement response of the PEA with respect to the driving voltage [21,29]. These characteristics motivate the use of phenomenological modeling approaches, which have proven effective in describing PEA hysteresis behavior [30,31]. Among them, the classical Prandtl–Ishlinskii (PI) model has been widely employed to characterize hysteresis nonlinearities and provides an analytical inverse suitable for feedforward compensation [32,33]. However, the conventional PI model cannot adequately represent rate-dependent and asymmetric hysteresis effects [21,34,35].

In this work, a frequency-scanning nonlinearity suppression method for FSI ranging based on a rate-dependent asymmetric Prandtl–Ishlinskii (RA-PI) model is proposed. For the first time, the phenomenological modeling approach is employed to characterize the rate-dependent and asymmetric optical frequency-scanning behavior of an ECDL. An inverse RA-PI model is derived and used as a feedforward compensator to generate pre-distorted driving voltages, enabling linearization of the frequency scanning. Compared with existing methods, the proposed approach accurately captures both asymmetry and rate dependence using a simple structure with low computational burden, without requiring additional hardware or complex post-processing. Experimental results show that the proposed method improves the frequency-scanning linearity of the ECDL by approximately one order of magnitude and enhances FSI performance for both static and dynamic targets. The proposed scheme provides a simple, efficient, and broadly applicable solution for frequency-scanning nonlinearity suppression in ECDL-based FSI system.

The remainder of this paper is structured as follows: Section 2 introduces the principle of FSI and analyzes the impact of frequency-scanning nonlinearity. Section 3 presents the phenomenological modeling approach based on the RA-PI model and the corresponding inverse feedforward compensation scheme. Experimental validation of frequency-scanning nonlinearity suppression is provided in Section 4, followed by evaluation of FSI ranging performance under static and dynamic conditions.

2. Principle

2.1. Principle of FSI

Figure 1 illustrates a schematic diagram of the proposed FSI ranging system. The F–P cavity and the auxiliary interferometer are used to obtain the variation pattern of the optical frequency. The time delay between the reference and measurement arms is defined as $\tau = 2nL/c$, where n is the air refractive index, L is the optical path difference (OPD), and c is the speed of light in vacuum.

Optics EXPRESS

The interference signal generated by the interferometer produces a voltage at a PD given by [12]

$$I(t) \propto \cos[\varphi(t)] = \cos[2\pi\upsilon(t)\tau(t)], \tag{1}$$

where $\upsilon(t)$ denotes the instantaneous optical frequency of the laser. When the optical frequency is scanned over a bandwidth $\Delta\upsilon$, the distance to target L can be determined as

$$L = \frac{c}{4\pi n} \cdot \frac{\Delta\varphi}{\Delta\upsilon} = \frac{c}{4\pi n} \cdot \frac{N \cdot 2\pi}{\Delta\upsilon} = \frac{c}{2n} \frac{N}{\Delta\upsilon}, \tag{2}$$

where N denotes the number of interference fringes counted during the frequency scanning. In practice, $\Delta\upsilon$ is obtained by counting the number of the F-P signal peaks, whose free spectral range (FSR) is known. Equation (2) indicates that accurate distance measurement in FSI relies on a linear relationship between the optical frequency and time. Deviations from linear frequency scanning introduce errors in fringe phase evolution, thereby degrading the ranging accuracy. This effect is analyzed in detail in the following subsection.

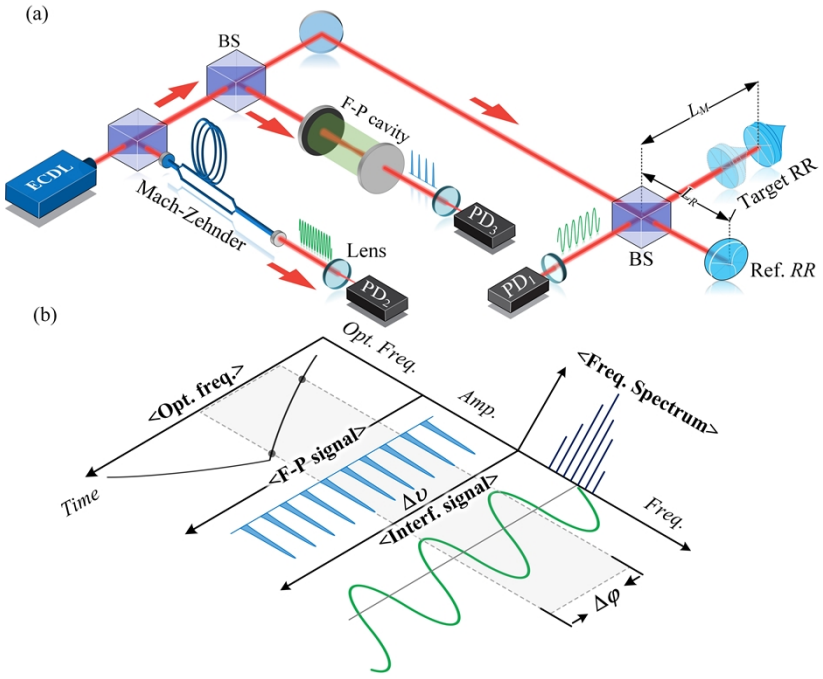

Fig. 1. Schematic illustration of the F-P cavity based FSI ranging.

2.2. *Laser frequency scanning nonlinearity in FSI*

Considering the presence of frequency-scanning nonlinearity, the frequency-scanning rate $d\upsilon/dt$ is no longer invariant. To facilitate analysis, the instantaneous optical frequency can be approximated by a second-order Taylor expansion as

$$\upsilon(t) = \upsilon_0 + \beta t + \gamma t^2, \tag{3}$$

where β and γ denote the linear and nonlinear components of the frequency scan, respectively, and υ_0 is the initial optical frequency. Substituting Eq. (3) into Eq. (1), the phase of the interference signal can be expressed as $\varphi(t) = 2\pi\tau(\upsilon_0 + \beta t + \gamma t^2)$. Consequently, the extracted phase difference

Optics EXPRESS

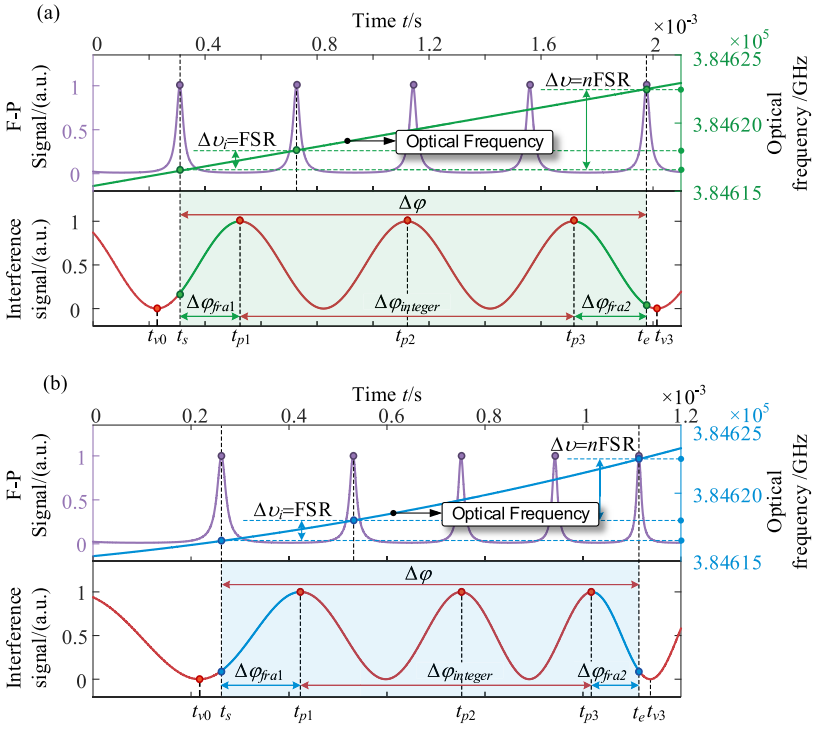

Fig. 2. Simulated phase evolution of the interference signal under (a) linear and (b) nonlinear laser frequency scanning. The linear and nonlinear frequency-scanning curves are indicated for comparison. Simulation parameters: $\lambda_0 = 780$ nm, FSR=1.5 GHz, $L = 0.07$ m, $\beta = 3600$ GHz/s, $\gamma = 2.5 \times 10^6$GHz^2/s, $n = 1$.

$\Delta\varphi$ deviates from the ideal linear evolution. Figure 2 illustrates the simulated phase evolution under linear and nonlinear frequency scanning, respectively.

The phase difference $\Delta\varphi$ can be decomposed into an integral part $\Delta\varphi_{\text{int}}$ and a fractional part $\Delta\varphi_{fra}$ which can be expressed as

$$\Delta\varphi = [(t_{p1} - t_s)/(t_{p1} - t_{v0}) + (t_e - t_{p3})/(t_{v3} - t_{p3})]\pi + 2\pi. \tag{4}$$

Frequency-scanning nonlinearity results in a nonlinear temporal evolution of the phase, as shown in Fig. 2(b). Consequently, the estimation of $\Delta\varphi_{fra}$ based on Eq. (4) becomes inaccurate, leading to a degradation in ranging accuracy.

In addition to phase distortion, frequency-scanning nonlinearity also causes spectral broadening of the interference signal. The resulting spectral peak width can be expressed as [13]

$$\delta f_b = \frac{(1 + 2\pi\tau\upsilon_{nl,rms})}{T_s} \tag{5}$$

where $\upsilon_{nl,rms} = \sqrt{\sum_{m=1}^{N} \upsilon_{nl}^2(m)/N}$ denotes the root mean square (RMS) value of the frequency-scanning nonlinearity and T_s is the frequency-scanning period. Accordingly, the ranging resolution can be written as

$$\delta L = \frac{c\delta f_b}{2\beta} = \frac{c(1 + 2\pi\tau\upsilon_{nl,rms})}{2\Delta\upsilon}. \tag{6}$$

When $2\pi\tau\upsilon_{nl,rms} \ll 1$, Eq. (6) reduces to the conventional bandwidth-limited resolution $\delta L = c/2\Delta\upsilon$. In contrast, when $\upsilon_{nl,rms}$ becomes non-negligible and the frequency-scanning

Optics EXPRESS

nonlinearity dominates, the nonlinearity-limited range resolution can be approximated as

$$\delta L = \frac{\pi c \tau \upsilon_{nl,rms}}{\Delta \upsilon}. \tag{7}$$

The above analysis demonstrates that frequency-scanning nonlinearity degrades both the ranging accuracy and resolution of FSI systems. Effective suppression of this nonlinearity is therefore essential for achieving high-precision absolute ranging. To this end, a novel frequency-scanning nonlinearity suppression method for ECDLs is proposed based on a phenomenological modeling approach.

3. Methodology

3.1. Rate-dependent asymmetric Prandtl–Ishlinskii model

The classical PI model incorporates Play operators to characterize the hysteresis nonlinearities of the PEA. The Play operator can be expressed as

$$\Gamma_r[u](t) = \max\{x(t) - r, \min\{x(t) + r, \Gamma_r[u](t-1)\}\}, \tag{8}$$

where $u(t)$ is the input and r is a positive threshold. The Input-output relationship of the Play operator is illustrated in Fig. 3(a). As observed, classical Play operators exhibit symmetric hysteresis loops and are therefore inadequate for accurately characterizing asymmetric hysteresis behavior.

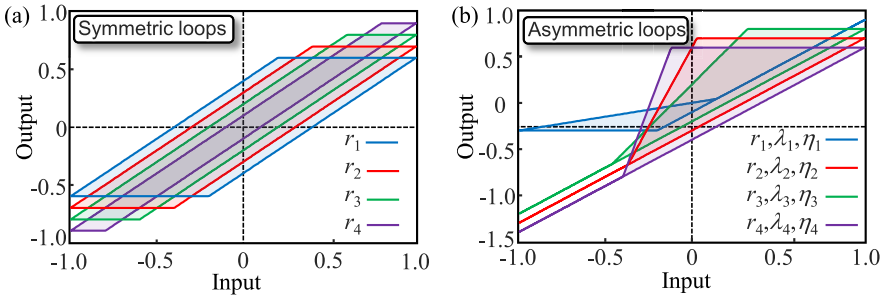

Fig. 3. (a) Symmetric hysteresis loops of the classical Play operator with different threshold values r_i (b) Asymmetric hysteresis loops of the asymmetric Play operator with different parameter sets (r_i, λ_i, η_i).

To address this issue, an asymmetric Play operator is introduced and defined as [29]

$$\Gamma_{r,\lambda,\eta}[u](t) = \max\{u(t) - r, \min\{\lambda u(t) + \eta r, \Gamma_{r,\lambda,\eta}[u](t-1)\}\}, \tag{9}$$

where the λ and η are shape-modifying coefficients of the asymmetric Play operator. As shown in Fig. 3(b), the asymmetric Play operator produces hysteresis loops with pronounced asymmetry. Specifically, λ and η respectively determine the slope and intercept of the hysteresis loop, while the degree of asymmetry is mainly governed by λ.

In the classical Play operator, r is rate-independent. To incorporate rate-dependent hysteresis behavior into the input–output relationship, a dynamic threshold related to the input signal frequency is introduced. Since the hysteresis width is governed by r, the dynamic threshold is defined as

$$r = \alpha + g(\dot{u}(t)), \tag{10}$$

where α represents the rate-independent hysteresis component, and $g(\dot{u}(t))$ characterizes the rate-dependent effect. The order for $g(\dot{u}(t))$ determines the trade-off between model accuracy and

Optics EXPRESS

complexity. In this study, a linear function is adopted, yielding

$$r(f_{in}) = \alpha u(f_{in}, t)_{pp}/2 + \zeta f_{in}, \tag{11}$$

where $u(f_{in}, t)_{pp}$ denotes the peak-to-peak value of the input signal, f_{in} is the input frequency, and α and ζ are control parameters. By incorporating the dynamic threshold, the rate-dependent API play operator is formulated as

$$\Gamma_{r,\lambda,\eta}[u](f_{in}, t) = \max\{u(f_{in}, t) - r, \min\{\lambda u(f_{in}, t) + \eta r, \Gamma_{r,\lambda,\eta}[u(f_{in}, t-1)]\}\}, \tag{12}$$

where $r = r(f_{in})$. To ensure that the initial value of the rate-dependent API play operator lies within the hysteresis loop, it is initialized as

$$\Gamma_{r,\lambda,\eta}[u](f_{in}, t_0) = \max\{u(f_{in}, t_1) - r, \lambda u(f_{in}, t_1) + \eta r\}, \tag{13}$$

where $u(f_{in}, t_1)$ denotes the minimum value of $u(f_{in}, t)$.

The schematic diagram of the proposed RA-PI model is illustrated in Fig. 4. The model consists of two components: a memory function and a memoryless function. The memory function is constructed as a weighted superposition of RA-Play operators and is expressed as

$$\mathrm{H}[u](f_{in}, t) = \sum_{i=1}^{N_1} p_i \cdot \Gamma_{r_i,\lambda_i,\eta_i}[u(f_{in}, t)], \tag{14}$$

where N_1 denotes the number of RA-Play operators, and $p_i = ae^{-br_i}$ is the weighting coefficient associated with the dynamic threshold r_i. The parameters a and b are weight control coefficients.

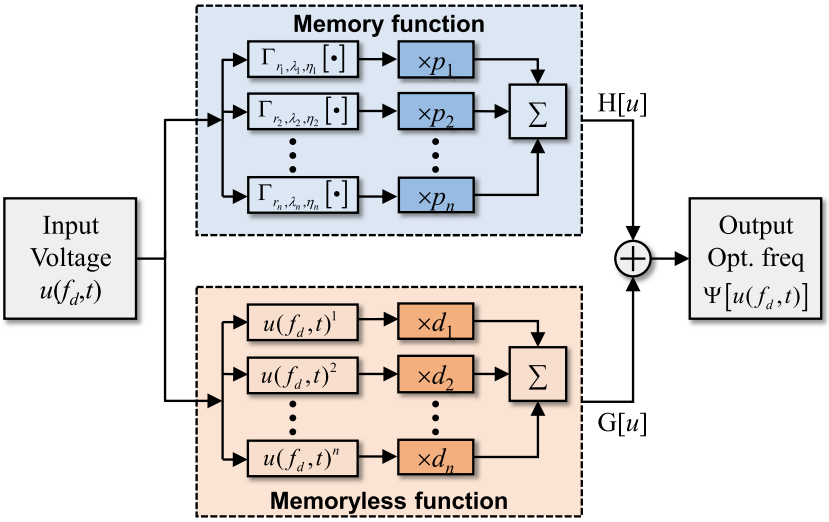

Fig. 4. The schematic diagram of the RA-PI model.

The memoryless function is modeled as a polynomial of the input signal and can be written as

$$G[u](f_{in}, t) = \sum_{i=1}^{N_2} d_i u^i(f_{in}, t), \tag{15}$$

where N_2 is the polynomial order and d_i are the corresponding polynomial coefficients. By combining the memory and memoryless functions, the rate-dependent and asymmetric hysteresis

Optics EXPRESS

nonlinearity is represented by the RA-PI model as

$$\Psi[u](f_{in},t) = \mathrm{H}[u](f_{in},t) + G[u](f_{in},t). \tag{16}$$

Consequently, when $u(f_{in},t)$ denotes the driving voltage applied to the ECDL and $\Psi[u](f_{in},t)$ represents the output optical frequency, the proposed RA-PI model provides an effective phenomenological representation of the rate-dependent and asymmetric frequency-scanning nonlinearities induced by the PEA in the ECDL system.

3.2. Inverse RA-PI model

In this study, an inverse RA-PI model is constructed as a feedforward compensator. Since a closed-form analytical inverse of the RA-PI model is not directly available, the inverse formulation is derived based on the analytical inverse of the classical PI model. The classical PI model admits an analytical inverse, in which the thresholds and weights of the inverse Play operators are transformed from those of the forward model [21,36]. The relationship between the thresholds z_i, weights q_i of the inverse PI model and those of the forward PI model are expressed is given by

$$\begin{cases} z_1 = p_0 r_1, z_{i+1} - z_i = \left(\sum_{j=0}^{i} p_j\right)(r_{i+1} - r_i) \\ q_0 = \frac{1}{p_0}, q_i = \frac{1}{\sum_{j=0}^{i} p_j} - \frac{1}{\sum_{j=0}^{i-1} p_j} \end{cases}, \tag{17}$$

where p_j and r_i denote the weights and thresholds of the forward PI model, respectively.

Owing to the structural consistency between the RA-PI model and the classical PI model, the inverse RA-PI model is constructed by extending the inverse PI formulation. The construction procedure is summarized as follows.

a. Equation (11) and (17) are combined to derive the inverse Play operators and construct the inverse PI model, as illustrated in Fig. 4.

b. The thresholds and weights of the inverse PI model are fitted to obtain compact parametric expressions.

$$\begin{cases} z_i = s_1 i^2 + s_2 i + s_3 \\ q_i = \sigma i^{\varepsilon} \end{cases}, \tag{18}$$

where s_1, s_2, s_3, are threshold control parameters, and σ and ε are weight control parameters.

c. To incorporate rate dependence, a linear frequency-dependent term is introduced into the threshold expression

$$z_i(f_{in}) = s_1 i^2 + s_2 i + s_3 + \kappa f_{in}, \tag{19}$$

where κ is the rate-dependent threshold control parameter.

d. The inverse RA-PI model retains the same structure as the forward RA-PI model. Accordingly, the RA-Play operator used in the inverse RA-PI model is defined as:

$$\Phi_{r,\lambda,\eta}[\upsilon](f_{in},t) = \max\{\upsilon(f_{in},t) - z, \min\{\lambda\upsilon(f_{in},t) + \eta z, \Gamma_{r,\lambda,\eta}[\upsilon](f_{in},t-1)\}\}, \tag{20}$$

where $z = z(f_{in})$, and $\upsilon(f_{in},t)$ represents the optical frequency input to the inverse model.

e. The memory and memoryless components of the inverse RA-PI model are expressed as

$$P[\upsilon](f_{in},t) = \sum_{i=1}^{N_1} q_i \cdot \Phi_{r_i,\lambda_i,\eta_i}[\upsilon](f_{in},t), \tag{21}$$

$$Q[\upsilon](f_{in},t) = \sum_{i=1}^{N_2} g_i \upsilon^i(f_{in},t). \tag{22}$$

Optics EXPRESS

The inverse RA-PI model is therefore written as

$$\Upsilon[\upsilon](f_{in},t) = P[\upsilon](f_{in},t) + Q[\upsilon](f_{in},t), \tag{23}$$

where $\Upsilon[\upsilon](f_{in},t)$ represents the driving voltage corresponding to the ECDL output $\upsilon(f_{in},t)$. When an ideal linear laser frequency-scanning trajectory $\upsilon_{id}(f_{in},t)$ is applied to the inverse model, the desired driving voltage is obtained as

$$u_d(f_{in},t) = \Upsilon[\upsilon_{id}](f_{in},t), \tag{24}$$

which provides the feedforward compensation for frequency-scanning nonlinearities in the ECDL.

3.3. Parameter identification of the RA-PI model

The rate-dependent frequency-scanning curves of the ECDL under triangular-wave voltage excitation at different driving frequencies are shown in Fig. 5(a). These measured curves are used as observation data for identifying the parameters of the RA-PI model and its inverse. The parameter identification scheme is illustrated in Fig. 5(b). The characterization error of the RA-PI model is defined as

$$e(t_k) = \Psi[u](f_{in},t_k) - \upsilon(f_{in},t_k), \tag{25}$$

where $u(f_{in},t_k)$ denotes measured driving voltage applied to the ECDL, and $\upsilon(f_{in},t_k)$ is the corresponding optical frequency measured by using an F–P cavity and an auxiliary interferometer [37]. $\Psi[u](f_{in},t_k)$ is the RA-PI model output when the input is $u(f_{in},t_k)$. The index k ($k = 1,\ldots,K$) represents the sampled data points within one complete frequency-scanning period. The parameter vector of the RA-PI model $X = \{\alpha,\zeta,\lambda_i,\eta,a,b,d_i,N_1,N_2\}$ is identified minimizing the weighted sum of squared characterization errors over different excitation frequencies

$$\Theta = \sum_{j=1}^{J}\sum_{k=1}^{K} A_j e(t_k)^2, \tag{26}$$

where Θ is the objective function, J denotes the number of excitation frequency cases, and A_j is a weighting factor determined by the hysteresis percentage of the measured frequency-scanning curve at the j_{th} excitation frequency, introduced to emphasize error minimization under higher excitation frequencies [36].

The model parameters are iteratively optimized to minimize the objective function Θ. The identified parameters, together with Eq. (19), are subsequently used to characterize the rate-dependent frequency-scanning behavior of the ECDL. The validity of the RA-PI model is evaluated by comparing the model output with the measured optical frequency curves, as shown in Fig. 6. The characterization performance is quantified using the root-mean-square error (RMSE)

$$\text{RMSE} = \sqrt{\frac{1}{K}\sum_{k=1}^{K}[\Psi[u](f_{in},t_k) - \upsilon(f_{in},t_k)]^2}. \tag{27}$$

The model output results indicate that the RA-PI model accurately reproduces the nonlinear frequency-scanning behavior over the considered excitation frequencies.

Parameter identification for the inverse RA-PI model follows the same procedure. In this case, the measured optical frequency curves $\upsilon(f_{in},t)$ are used as inputs, while the corresponding driving voltages $u(f_{in},t)$ serve as observation data. The characterization error of the inverse model is

Optics EXPRESS

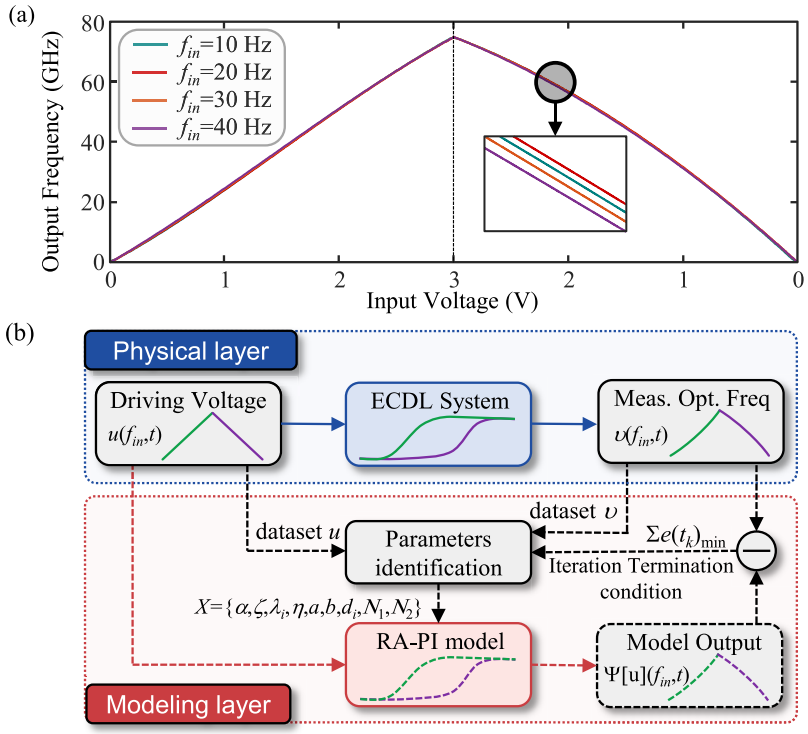

Fig. 5. (a) Measured rate-dependent frequency-scanning curves of the ECDL under triangular-wave voltage excitation at different driving frequencies. (b) Schematic of the parameter identification procedure for the RA-PI model.

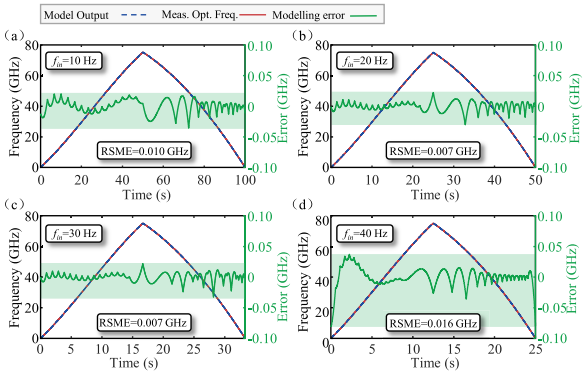

Fig. 6. Comparison between the RA-PI model output and the measured optical frequency curves at excitation voltage frequencies of (a) 10 Hz, (b) 20 Hz, (c) 30 Hz, and (d) 40 Hz.

Optics EXPRESS

defined as

$$e_I(t_k) = \Upsilon[\upsilon](f_{in}, t_k) - u(f_{in}, t_k), \tag{28}$$

where $\Upsilon[\upsilon](f_{in}, t_k)$ is the inverse RA-PI model output. The parameter vector of inverse RA-PI model is $X = \{s_1, s_2, s_3, \sigma, \varepsilon, \lambda_i, \eta, g_i, N_1, N_2, \kappa\}$ and the objective function is given as

$$\Theta_I = \sum_{j=1}^{J} \sum_{k=1}^{K} A_j e_I(t_k)^2. \tag{29}$$

The inverse model parameters are obtained by minimizing the associated objective function. The optimized inverse RA-PI model is subsequently employed as a feedforward compensator to determine the pre-distorted driving voltage for the ECDL. The validity of the inverse model is evaluated by comparing the model output with the measured driving voltage, as shown in Fig. 7. The identified parameters of the inverse RA-PI model remain valid over the considered range of excitation frequencies.

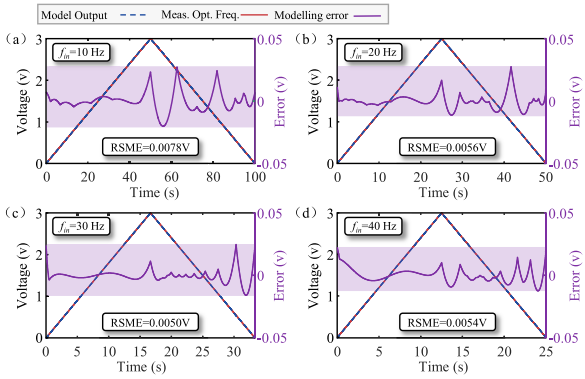

Fig. 7. Comparison between the inverse RA-PI model output and the measured driving voltage of ECDL at excitation voltage frequencies of (a) 10 Hz, (b) 20 Hz, (c) 30 Hz, and (d) 40 Hz.

4. Experimental results

4.1. Frequency-scanning nonlinearity compensation

We experimentally evaluated the inverse RA-PI model as a feedforward compensator to suppress the rate-dependent frequency-scanning nonlinearities of a commercial ECDL (Newport TLB6712, 780 nm). Figure 8 illustrates the compensation principle. The inverse model generated a pre-distorted driving voltage based on an ideal linear trajectory. This voltage was applied to the ECDL, and the resulting frequency scan was measured via the beat signal phase of an auxiliary MZI (containing a 5-m SMF reference arm) using the Hilbert Transform (HT) according to $\upsilon(t) = \varphi(t)/2\pi\tau$ [23]. The nonlinearity suppression was assessed using the frequency-scanning nonlinearity $1 - r^2$, which is defined as $1 - r^2 = 12(\upsilon_{nl,rms}/\Delta\upsilon)^2$ [38].

The ECDL was driven by AC voltages at 10, 20, 30, and 40 Hz (superimposed on a 3 V DC bias), yielding a ~75 GHz bandwidth. Beat signals were recorded by a 30 MS/s digitizer (NI PXIe-5105). To mitigate edge effects caused by the PEA's dynamic response in the transition regions of the up and down scans, we analyzed the region of interest (ROI), defined as the middle 80% (approx. 60 GHz) of the scanning range.

Figures 9(a) and 9(b) compare the frequency-scanning curves with and without compensation. The uncompensated scan exhibits significant rate-dependent nonlinearity as shown in Fig. 9(c),

Optics EXPRESS

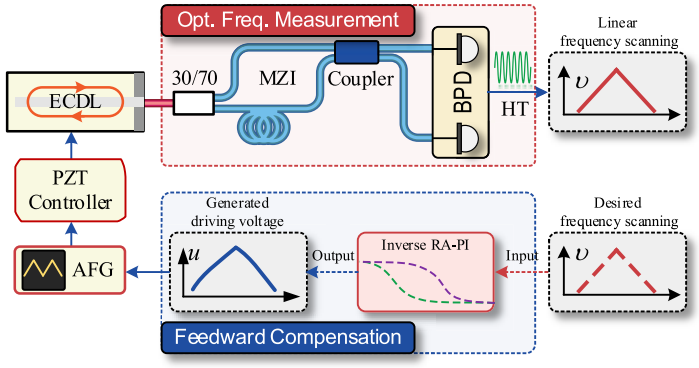

Fig. 8. Schematic of the frequency-scanning nonlinearity suppression principle using the inverse RA-PI model.

which is effectively suppressed by the feedforward control as shown in Fig. 9(d). Table 1 summarizes quantitative performance metrics. For the up-scan segments, the values $\upsilon_{nl,rms}$ were reduced by an order of magnitude (e.g., from 4.35×10^{8} Hz to 6.37×10^{7} Hz at 10 Hz). Correspondingly, significant reductions were observed in the down-scan segments (e.g., from 3.28×10^{9} Hz to 2.71×10^{8} Hz at 10 Hz). The maximum residual nonlinearity was reduced to 0.13% and 0.48% of the frequency excursion for the scan-up and scan-down segments, respectively. Furthermore, the $1-r^2$ values were improved from 10^{-4} to 10^{-5} for up-scan and 10^{-2} to 10^{-4} for down-scan. According to Eq. (7), the corresponding range resolution was improved by at least 5.28 and 12.1 times for the scan-up and scan-down segments.

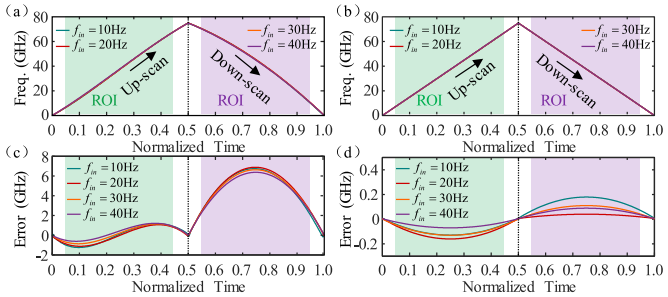

Fig. 9. Comparison of ECDL frequency-scanning curves with and without inverse RA-PI model compensation. (a) frequency-scanning curves without compensation, (b) frequency-scanning curves with compensation, (c) residual nonlinearity errors without compensation, and (d) compensated residual nonlinearity errors with compensation.

Spectral analysis of the scanning interference signals is presented in Fig. 10. Without compensation, significant spectral peak broadening was observed. After applying inverse RA-PI feedforward compensation, the spectral peak widths were reduced by approximately 10.93, 12.77, 31.25, and 16.75 times at excitation frequencies of 10, 20, 30, and 40 Hz, respectively, confirming effective suppression of frequency-scanning nonlinearity.

Long-term stability was evaluated by monitoring the frequency-scanning linearity over a continuous 120-minute measurement period as shown in Fig. 11. The standard deviations of the nonlinearity metric $\upsilon_{nl,rms}$ were 2.34 MHz and 2.57 MHz for the up-scan and down-scan segments, respectively, indicating stable compensation performance over extended operation.

Optics EXPRESS

Table 1. Frequency-scanning nonlinearity metrics without and with compensation

f_{in} (Hz)	Without compensation				With compensation			
	$\upsilon_{nl,rms}$ (Hz)		$1-r^2$		$\upsilon_{nl,rms}$ (Hz)		$1-r^2$	
	Up ($\times10^8$)	Down ($\times10^9$)	Up ($\times10^{-4}$)	Down ($\times10^{-2}$)	Up ($\times10^7$)	Down ($\times10^8$)	Up ($\times10^{-5}$)	Down ($\times10^{-4}$)
10	4.35	3.28	7.15	4.26	6.37	2.71	1.64	2.97
20	4.00	3.24	6.12	4.23	7.58	2.43	2.31	2.39
30	3.91	3.12	5.83	3.92	6.19	1.79	1.55	1.30
40	4.00	3.03	6.15	3.70	3.38	1.54	0.460	0.967

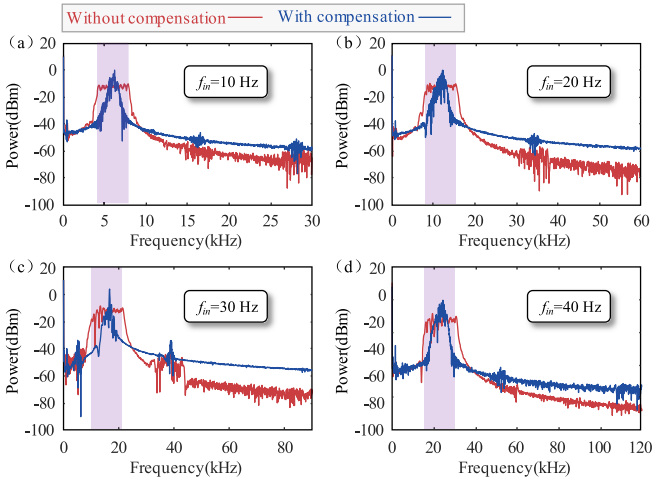

Fig. 10. Comparison of spectral peak widths in beat signals with and without frequency scanning nonlinearity compensation, measured under excitation frequencies of (a) 10 Hz, (b) 20 Hz, (c) 30 Hz, and (d) 40 Hz.

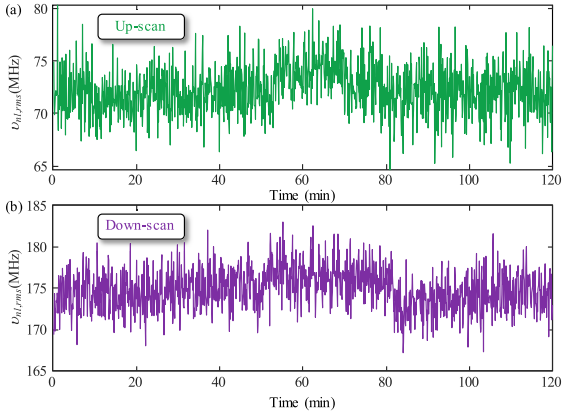

Fig. 11. Long-term stability of frequency scanning linearity over a 120-minute measurement period.

Optics EXPRESS

4.2. FSI ranging performance

To evaluate the impact of frequency-scanning nonlinearity compensation on ranging performance, the proposed inverse RA-PI feedforward scheme was integrated into an FSI measurement system, as shown in Fig. 12. The experiments were conducted using a target prism mounted on a motorized linear translation stage (Newport M-ILS200LM-S, travel range: 200 mm, repeatability accuracy: ±0.12 μm). The pre-distorted driving voltage generated by the inverse RA-PI model was applied to the ECDL via an arbitrary function generator (Tektronix AFG31052). The laser frequency scanning range was monitored using an F–P cavity (Thorlabs SA200).

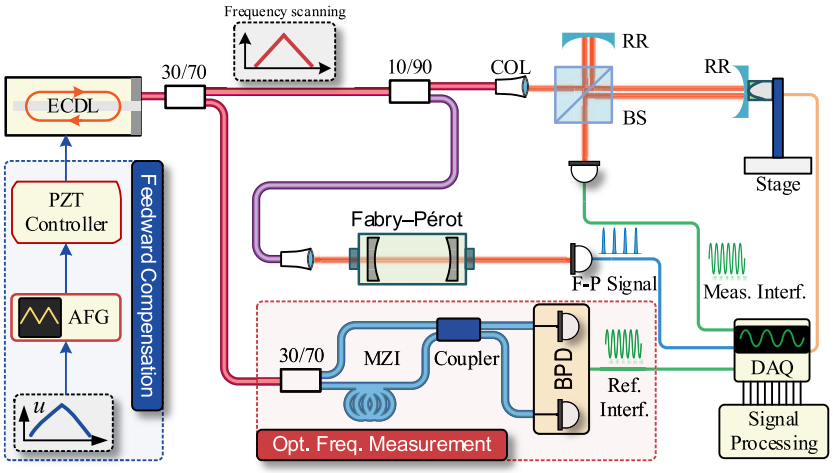

Fig. 12. Experimental setup of the FSI measurement system.

Static measurements were performed by moving the target in equidistant steps of 20 mm across ten measurement nodes. Each node was measured for 5 s under stabilized conditions. Distance values were calculated according to Eq. (4), and a Kalman filter-based dynamic FSI processing method was applied to suppress vibration-induced fluctuations [39]. Figure 13(a) shows the measured distances and corresponding standard deviations (STDs) without and with compensation, for clarity, the error bars are magnified by a factor of 1000. The numerical results are summarized in Table 2. After applying frequency-scanning nonlinearity compensation, the STDs at all measurement nodes were significantly reduced, with the maximum STD decreasing from 58.25 μm to 9.79 μm. Relative displacement between adjacent nodes was further evaluated, with results shown in Fig. 13(b) and summarized in Table 3. The displacement deviations were markedly reduced after compensation, with the maximum deviation decreasing from 42.97 μm to 11.56 μm. These results indicate improved stability and accuracy of static FSI measurements.

Dynamic measurements were assessed by measuring a moving target driven at constant velocities of 5, 10, 20, 30, 40, and 50 mm/s. Each velocity condition was maintained for 2 s. Distance trajectories without and with compensation are shown in Fig. 14(a) and Fig. 14(b), respectively. The velocity was estimated from the slope of the measured distance curves using the Kalman filter-based dynamic FSI method [39]. The deviations between measured and reference velocities are illustrated in Fig. 14(c), and quantitative results are summarized in Table 4. After compensation, velocity measurement deviations were reduced by factors ranging from 2.61 to 5.75 across different motion speeds. Overall, the results indicate that suppressing frequency-scanning nonlinearity using the inverse RA-PI feedforward compensator improves both static and dynamic ranging performance of the FSI system.

Optics EXPRESS

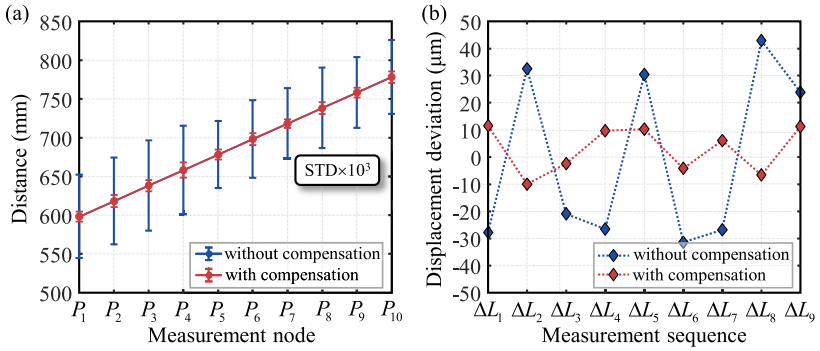

Fig. 13. Experimental results for static measurements. (a) Measured distances without and with compensation and corresponding STDs (magnified by a factor of 10-3 for clarity). (b) Displacement deviations between adjacent measurement nodes without and with compensation.

Table 2. Distance measurements and STDs without and with compensation

P_i	Without compensation		With compensation	
	$L_i(m)$	STD(μm)	$L_i(m)$	STD(μm)
1	598.3928	53.68	598.3004	6.65
2	618.3650	55.98	618.3120	7.85
3	638.3975	58.25	638.3020	7.20
4	658.3766	57.10	658.2996	9.79
5	678.3501	43.26	678.3094	6.41
6	698.3805	50.03	698.3196	7.72
7	718.3491	45.61	718.3155	5.65
8	738.3223	51.92	738.3215	7.61
9	758.3653	45.58	758.3149	6.15
10	778.3892	47.86	778.3262	7.57

Table 3. Displacement deviations with and without compensation

ΔL_j	With compensation		Without compensation	
	ΔL_j(mm)	Deviation(μm)	ΔL_j(mm)	Deviation(μm)
1	19.9722	-27.77	20.0116	11.56
2	20.0325	32.54	19.9901	-9.99
3	19.9790	-20.97	19.9977	-2.37
4	19.9735	-26.50	20.0098	9.77
5	20.0304	30.43	20.0102	10.23
6	19.9686	-31.41	19.9958	-4.16
7	19.9732	-26.76	20.0061	6.07
8	20.0430	42.97	19.9934	-6.63
9	20.0240	23.93	20.0113	11.29

Optics EXPRESS

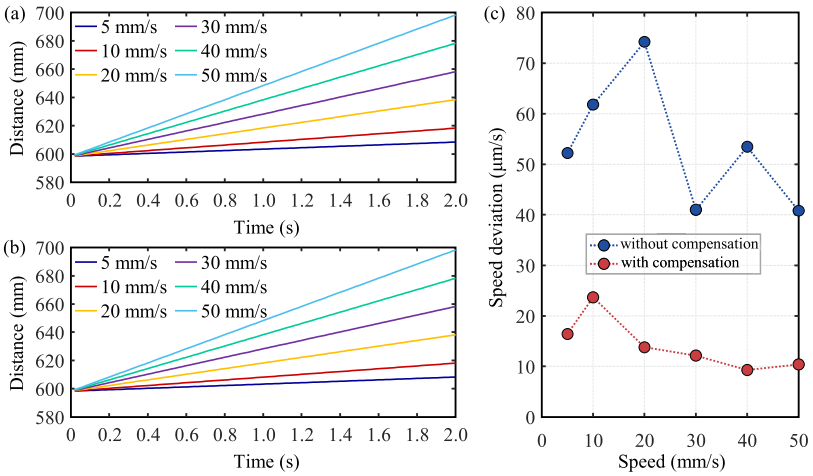

Fig. 14. Experimental results for dynamic measurements. Distance trajectories (a) without compensation and (b) with compensation. (c) Velocity measurement deviations with and without compensation.

Table 4. Velocity measurements and deviations with and without compensation

Speed (mm/s)	With compensation		Without compensation	
	Average speed (mm/s)	Deviation (μm/s)	Average speed (mm/s)	Deviation (μm/s)
5	5.052238	52.24	5.016437	16.44
10	9.938197	61.80	9.976349	23.65
20	20.074228	74.23	19.986211	13.79
30	30.040987	40.99	30.012140	12.14
40	40.053478	53.48	39.990702	9.30
50	50.040809	40.81	50.010413	10.41

5. Conclusion and discussion

In this work, inspired by the effectiveness of the classical PI model in characterizing PEA hysteresis, we proposed, for the first time, a frequency-scanning nonlinearity suppression method for ECDLs based on a phenomenological modeling approach. Considering the rate-dependence and the pronounced asymmetry between the up- and down-scanning segments of the ECDL optical frequency response, we introduced an RA-PI model to accurately characterize the nonlinear optical frequency tuning behavior. We derived an inverse RA-PI model and implemented it as a feedforward compensator to linearize the optical frequency scanning of the ECDL. Experimental results demonstrate that the proposed method improves the frequency-scanning linearity by approximately one order of magnitude. Consequently, the maximum standard deviation of absolute distance measurements was reduced from 58.25 μm to 9.79 μm, and the maximum relative displacement deviation decreased from 42.97 μm to 11.56 μm. For dynamic targets, velocity measurement deviations were reduced by factors ranging from 2.61 to 5.75, confirming enhanced performance for both static and dynamic FSI ranging. This study provides a simple, efficient, and broadly applicable solution for high-precision coherent measurement, with potential applicability to related platforms such as LiDAR, OCT, and OFDR.

Despite these improvements, it should be noted that a strictly closed-form inverse for the RA-PI model is currently unavailable. The inverse formulation adopted in this study is derived

Optics EXPRESS

based on the analytical inverse structure of the classical PI model, which may, to a certain extent, limit the theoretical precision of the feedforward compensation. Future work will focus on refining the inverse modeling methodology to further improve modeling accuracy and nonlinearity suppression performance.

Furthermore, while the RA-PI model was initially developed to address the specific frequency-scanning nonlinearity of ECDLs, it is fundamentally a phenomenological modeling approach. As such, the model's structure remains agnostic to the underlying physical mechanisms and instead focuses on characterizing observed rate-dependent and asymmetric hysteresis behaviors. Consequently, despite the distinct physical origins of frequency-scanning nonlinearity in DFB lasers and VCSELs, the proposed method is expected to be readily applicable to modeling and suppressing nonlinearities in these sources. Additionally, we plan to implement this frequency-scanning nonlinearity suppression algorithm on FPGA platforms, to facilitate real-time operation and broaden its engineering applications.

Funding. National Natural Science Foundation of China (52205576); Optoelectronic Measurement and Intelligent Perception Zhongguancun Open Lab (No. LabSOMP-2023-04); Key Research and Development Projects of Shaanxi Province (No.2025CY-YBXM-121); State Key Laboratory for Manufacturing Systems Engineering (No. klms2021005); Natural Science Basic Research Program of Shaanxi (No. 2025JC-YBMS-016).

Disclosures. The authors declare no conflicts of interest.

Data availability. Data underlying the results presented in this paper are not publicly available at this time but may be obtained from the authors upon reasonable request.

References

1. J. J. Martinez, M. A. Campbell, M. S. Warden, *et al.*, "Dual-sweep frequency scanning interferometry using four wave mixing," IEEE Photonics Technol. Lett. **27**(7), 733–736 (2015).
2. J. Dale, B. Hughes, A. J. Lancaster, *et al.*, "Multi-channel absolute distance measurement system with sub ppm-accuracy and 20 m range using frequency scanning interferometry and gas absorption cells," Opt. Express **22**(20), 24869–24893 (2014).
3. M. Cui, M. G. Zeitouny, N. Bhattacharya, *et al.*, "High-accuracy long-distance measurements in air with a frequency comb laser," Opt. Lett. **34**(13), 1982–1984 (2009).
4. B. L. Swinkels, N. Bhattacharya, and J. J. M. Braat, "Correcting movement errors in frequency-sweeping interferometry," Opt. Lett. **30**(17), 2242–2244 (2005).
5. J. Zheng, L. Jia, Y. Zhai, *et al.*, "High-precision silicon-integrated frequency-modulated continuous wave lidar calibrated using a microresonator," ACS Photonics **9**(8), 2783–2791 (2022).
6. L. Cheng, X. Ziyi, L. Guodong, *et al.*, "Dynamic nonlinearity errors in laser Doppler vibrometer measurements induced by environmental vibration and error correction," Opt. Express **30**(17), 30705–30717 (2022).
7. Z. Wang, Z. Liu, K. Tian, *et al.*, "Frequency-scanning interferometry for dynamic measurement using adaptive Sage-Husa Kalman filter," Optics and Lasers in Engineering **165**, 107545 (2023).
8. H. Dang, Y. Tian, H. Liu, *et al.*, "Dynamic wavelength calibration based on synchrosqueezed wavelet transform," Opt. Express **30**(26), 46722–46733 (2022).
9. T. Xu, Y. Liu, J. Cui, *et al.*, "Calibration methods of optical path difference in optical frequency scanning interferometry with resampling resolving," Measurement **248**, 116854 (2025).
10. R. Bao, F. Duan, X. Fu, *et al.*, "Frequency-scanning interferometry for axial clearance of rotating machinery based on speed synchronization and extended Kalman filter," Opt Laser Eng. **164**, 107515 (2023).
11. W. Chen, X. Li, Z. Deng, *et al.*, "A phase jump phenomenon within the beat signal for dynamic target measurement in frequency-sweeping interferometry," Appl. Phys. Lett. **127**, 081103 (2025).
12. Z. Deng, W. Chen, L. Li, *et al.*, "Decoupling composite modulation models in frequency-scanning interferometry for dynamic absolute ranging using a multi-synchrosqueezing transform," Appl. Opt. **64**(13), 3554–3560 (2025).
13. X. Zhang, J. Pouls, M. C. Wu, *et al.*, "Laser frequency sweep linearization by iterative learning pre-distortion for FMCW LiDAR," Opt. Express **27**(7), 9965–9974 (2019).
14. J. Riemensberger, A. Lukashchuk, M. Karpov, *et al.*, "Massively parallel coherent laser ranging using a soliton microcomb," Nature **581**(7807), 164–170 (2020).
15. Z. Wang, B. Potsaid, L. Chen, *et al.*, "Cubic meter volume optical coherence tomography," Optica **3**(12), 1496–1503 (2016).
16. Y. Zhu, Z. Wang, K. Tian, *et al.*, "Phase-generated carrier combined with the Hilbert transform for phase demodulation in frequency-scanning interferometry," Opt. Laser Eng. **153**, 106988 (2022).
17. J. Zhu, D. Qiao, A. Jones, *et al.*, "1.7 THz tuning range pivot-point-independent mode-hop-free external cavity diode laser," Opt. Express **31**(3), 3970–3983 (2023).
18. R. Qian, J. Guo, Z. Wang, *et al.*, "Phase extraction method resistant to the nonlinearity for dynamic frequency scanning interferometry," Opt. Express **32**(21), 37516–37531 (2024).

Optics EXPRESS

19. L. Perret, P. Pfeiffer, N. Javahiraly, *et al.*, "Origin and control of sinusoidal nonlinearities in wavelength-tuned littman external cavity laser diodes," J. Lightwave Technol. **27**(22), 4927–4934 (2009).
20. Z. Deng, Z. Liu, B. Li, *et al.*, "Precision improvement in frequency-scanning interferometry based on suppressing nonlinear optical frequency sweeping," Opt. Rev. **22**(5), 724–730 (2015).
21. M. Al Janaideh, S. Rakheja, and C.-Y. Su, "Experimental characterization and modeling of rate-dependent hysteresis of a piezoceramic actuator," Mechatronics **19**(5), 656–670 (2009).
22. Guang Shi, Fumin Zhang, Xinghua Qu, *et al.*, "High-resolution frequency-modulated continuous-wave laser ranging for precision distance metrology applications," Opt Eng. **53**(12), 122402 (2014).
23. K. Yuksel, M. Wuilpart, and P. Mégret, "Analysis and suppression of nonlinear frequency modulation in an optical frequency-domain reflectometer," Opt. Express **17**(7), 5845–5851 (2009).
24. L. Jia, Y. Wang, X. Wang, *et al.*, "Nonlinear calibration of frequency modulated continuous wave LIDAR based on a microresonator soliton comb," Opt. Lett. **46**(5), 1025–1028 (2021).
25. P. A. Roos, R. R. Reibel, T. Berg, *et al.*, "Ultrabroadband optical chirp linearization for precision metrology applications," Opt. Lett. **34**(23), 3692–3694 (2009).
26. S. Kakuma, "Frequency-modulated continuous-wave laser radar using dual vertical-cavity surface-emitting laser diodes for real-time measurements of distance and radial velocity," Opt. Rev. **24**(1), 39–46 (2017).
27. M. Minissale, T. Zanon-Willette, I. Prokhorov, *et al.*, "Nonlinear frequency-sweep correction of tunable electromagnetic sources," IEEE Trans. Ultrason., Ferroelect., Freq. Contr. **65**(8), 1487–1491 (2018).
28. C. J. Karlsson and F. Å. A. Olsson, "Linearization of the frequency sweep of a frequency-modulated continuous-wave semiconductor laser radar and the resulting ranging performance," Appl. Opt. **38**(15), 3376–3386 (1999).
29. W. Wang, R. Wang, Z. Chen, *et al.*, "A new hysteresis modeling and optimization for piezoelectric actuators based on asymmetric Prandtl-Ishlinskii model," Sensors and Actuators A: Physical **316**, 112431 (2020).
30. Y. Cao and X. B. Chen, "A survey of modeling and control issues for piezo-electric actuators," J Dyn Syst-T Asme **137**(1), 014001 (2015).
31. M. Rakotondrabe, C. Clévy, P. Lutz, *et al.*, "Complete open loop control of hysteretic, creeped, and oscillating piezoelectric cantilevers," IEEE Trans. Automat. Sci. Eng. **7**(3), 440–450 (2010).
32. M. Al Janaideh, S. Rakheja, C.-Y. Su, *et al.*, "An analytical generalized prandtl-ishlinskii model inversion for hysteresis compensation in micropositioning control," IEEE/ASME Trans. Mechatron. **16**(4), 734–744 (2011).
33. S. Liu and C.-Y. Su, "A modified generalized Prandtl-Ishlinskii model and its inverse for hysteresis compensation," in *2013 American Control Conference*, (IEEE, 2013), 4759–4764.
34. G. Song, J. Zhao, X. Zhou, *et al.*, "Tracking control of a piezoceramic actuator with hysteresis compensation using inverse Preisach model," IEEE/ASME Trans. Mechatron. **10**(2), 198–209 (2005).
35. Y. Yu, Z. Xiao, N. G. Naganathan, *et al.*, "Dynamic Preisach modelling of hysteresis for the piezoceramic actuator system," Mechanism and Machine Theory **37**, 75–89 (2002).
36. M. Al Janaideh and P. Krejci, "Inverse rate-dependent Prandtl–Ishlinskii model for feedforward compensation of hysteresis in a piezomicropositioning actuator," IEEE/ASME Trans. Mechatron. **18**(5), 1498–1507 (2013).
37. Z. Deng, Z. Liu, X. Jia, *et al.*, "Dynamic cascade-model-based frequency-scanning interferometry for real-time and rapid absolute optical ranging," Opt. Express **27**(15), 21929–21945 (2019).
38. W. Chen, X. Li, Z. Deng, *et al.*, "Data-driven model based self-adaptive frequency-sweeping linearization in frequency-sweeping interferometry for absolute distance measurement," Measurement **253**, 117742 (2025).
39. L. Tao, Z. Liu, W. Zhang, *et al.*, "Frequency-scanning interferometry for dynamic absolute distance measurement using Kalman filter," Opt. Lett. **39**(24), 6997–7000 (2014).